with the sensory systems of consciousness. Br. J. Psychiatry 174, 196–204.

Ford, J.M., Mathalon, D.H., Kalba, S., Whitfield, S., Faustman, W.O., Roth, W.T., 2001a. Cortical responsiveness during talking and listening in schizophrenia: an event-related brain potential study. Biol. Psychiatry 50, 540–549.

Ford, J.M., Mathalon, D.H., Kalba, S., Whitfield, S., Faustman, W.O., Roth, W.T., 2001b. Cortical responsiveness during inner speech in schizophrenia: an event-related potential study. Am. J. Psychiatry 158, 1914–1916.

Ford, J.M., Mathalon, D.H., Heinks, T., Kalba, S., Faustman, W.O., Roth, W.T., 2001c. Neurophysiological evidence of corollary discharge dysfunction in schizophrenia. Am. J. Psychiatry 158, 2069–2071.

Frith, C., 1995. Functional imaging and cognitive abnormalities. Lancet 346, 615–620.

Muller-Preuss, P., Ploog, D., 1981. Inhibition of auditory cortical neurons during phonation. Brain Res. 215, 61–76.

Numminen, J., Curio, G., 1999. Differential effects of overt, covert and replayed speech on vowel-evoked responses of the human auditory cortex. Nurosci. Lett. 272, 29–32.

Numminen, J., Salmelin, R., Hari, R., 1999. Subject's own speech reduced reactivity of the human auditory cortex. Nurosci. Lett. 265, 119–122.

Oldfield, R.C., 1971. The assessment and analysis of handedness: the Edinburgh inventory. Neuropsychologia 9, 97–113.

Paus, T., Marrett, S., Worsley, K., Evans, A., 1996a. Imaging motor-to-sensory discharges in the human brain: an experimental tool for the assessment of functional connectivity. Neuroimage 4, 78–86.

Paus, T., Perry, D.W., Zatorre, R.J., Worsley, K.J., Evans, A.C., 1996b. Modulation of cerebral blood flow in the human auditory cortex during speech: Role of motor-to-sensory discharges. Eur. J. Neurosci. 8, 2236–2246.

Reite, M., Sheeder, J., Teale, P., Adams, M., Richardson, D., Simon, J., Jones, R.H., Rojas, D.C., 1997. Magnetic source imaging evidence of sex differences in cerebral lateralization in schizophrenia. Arch. Gen. Psychiatry 54, 433–440.

Turetsky, B.I., Colbath, E.A., Gur, R.E., 1998. P300 subcomponent abnormalities in schizophrenia. I. Physiological evidence for gender and subtype specific differences in regional pathology. Biol. Psychiatry 43, 84–96.

Topography of the Human Corpus Callosum Using Diffusion Tensor Tractography

Osamu Abe, MD, DMSc, Yoshitaka Masutani, PhD,* Shigeki Aoki, MD, DMSc,* Hidenori Yamasue, MD,† Haruyasu Yamada, MD,* Kiyoto Kasai, MD,† Harushi Mori, MD,* Naoto Hayashi, MD, DMSc,* Tomohiko Masumoto, MD,* and Kuni Ohtomo, MD, DMSc**

Objective: To evaluate the crossing fiber trajectory through the corpus callosum using distortion-corrected diffusion tensor tractography in the human brain.

Methods: After correcting distortion associated with large-diffusion gradients, T2-weighted echo planar images (EPIs) acquired from 10 right-handed healthy men were coregistered into T2-weighted fast spin echo images using linear through sixth-order nonlinear, 3-dimensional, polynomial warping functions. The optimal transformation parameters were also applied to the distortion-corrected diffusion-weighted EPIs. Diffusion tensor tractography through the corpus callosum was reconstructed, employing the "1 or 2 regions of interest" method.

Results: Compared with the lines through the genu, those through the rostrum ran more inferiorly and seemed to enter the orbital gyrus. Those lines entering posterior temporal white matter (tapetum) crossed through the ventral portion of the splenium and were clearly distinguished from lines that reached parieto-occipital white matter (forceps major).

Conclusion: Diffusion tensor tractography is a feasible noninvasive tool to evaluate commissural fiber trajectory.

Key Words: corpus callosum, brain, anatomy, magnetic resonance imaging, diffusion tensor tractography

(*J Comput Assist Tomogr* 2004;28:533–539)

Diffusion tensor imaging is a newer noninvasive magnetic resonance imaging (MRI) method that provides a means of characterizing the diffusivity of water molecules in the human brain and more pertinent insights into tissue structure, orientation, and temperature not accessible with conventional MRI sequences.[1,2] Diffusion tensor imaging has found application in a wide range of clinical situations such as acute cerebral ischemia, multiple sclerosis, brain maturation, and normal aging.[3–6] It is difficult to visualize the 3-dimensional information of the diffusion tensor into a 2-dimensional imaging plane, however. The means to express diffusion tensor data sets are mean diffusivity, an anisotropy index such as fractional anisotropy (FA),[7] a directionally encoded color map,[8] a vector map, and diffusion tensor tractography (DTT).[9–13] Diffusion tensor tractography reconstructs the 3-dimensional trajectories of white matter tracts, generally by following a continuous path of the greatest diffusivity through the brain from an initial set of seed points. It enables elicitation of white matter connectivity in vivo and is a promising tool to noninvasively elucidate normal neural fiber integrities and those changes in various disease processes.

Diffusion tensor tractography, however, has a few weak points. The first problem is a false-positive line tracking. Water diffuses preferentially along the axis of the fiber bundles, and DTT traces lines depending on the principal axis of the eigenvector associated with the largest eigenvalue of the diffusion tensor. Therefore, DTT does reconstruct lines between the neural fibers, which exist closely and have similar principal axes even when those are not actually interconnected. The second problem is a false-negative line tracking. Because voxel size observed with MRI is much larger than neural fibers, 2 or more white matter fiber bundles with different principal axes intersect within a voxel. As a result, the estimated axis of the first eigenvector is different from the principal axis of each fiber, resulting in early termination or deviation of tracking. Third, there is no gold standard of verifying the accuracy of drawn lines obtained with DTT in individual subjects.

Despite these problems, highly reproducible results in the corpus callosum consistent with those of previous postmortem investigations[15–18] have been shown in the several DTT studies.[10,11,13,14] There is no report to investigate the subdivided topography of the corpus callosum using DTT, however. The purpose of this study is to determine the topographic or-

From the *Department of Radiology, Graduate School of Medicine, University of Tokyo, Tokyo, Japan, and †Department of Neuropsychiatry, Graduate School of Medicine, University of Tokyo, Tokyo, Japan.

Supported in part by a Grant-in-Aid for Scientific Research (C) (2) 15591259 of the Ministry of Education, Science, Sports, and Culture of Japan.

Reprints: Dr Osamu Abe, Department of Radiology, Graduate School of Medicine, University of Tokyo, 7-3-1 Hongo Bunkyo-ku, Tokyo 113-8655, Japan (e-mail: abediag-tky@umin.ac.jp).

ganization of fibers coursing through the human corpus callosum using DTT in comparison with neuroanatomic knowledge.

MATERIALS AND METHODS

Subjects

Diffusion tensor imaging data were acquired from the cranium of 10 right-handed healthy men (24–36 years old, average age: 29.1 ± 4.3 years) without brain morphologic abnormalities, neurologic illness, head trauma, loss of consciousness, or psychiatric disorders. Written informed consent was obtained from all subjects according to the Declaration of Helsinki, and the scanning protocol was approved by the local ethical committee at our institution.

MRI Acquisition Protocol

All scans were acquired on a 1.5-T Signa Echo Speed MRI system (General Electric Medical Systems, Milwaukee, WI). A circularly polarized head coil was used for radiofrequency transmission and reception of the nuclear magnetic resonance signal. The pulse sequence we used in this study was single-shot, diffusion-weighted, echo planar acquisition (repetition time/echo time = 6000/78.2 milliseconds; numbers of excitation (NEX) = 4; acquisition time = 5 minutes, 36 seconds; matrix = 128 × 128; field of view = 240 mm × 240 mm; slice thickness = 5 mm; no gap; b value = 1000 s/mm^2; diffusion gradient directions = [0, 0, 0], [1/√2, 0, 1/√2], [−1/√2, 0, 1/√2], [0, 1/√2, 1/√2], [0, 1/√2, −1/√2], [1/√2, 1/√2, 0], and [−1/√2, 1/√2, 0]). We also acquired proton density–weighted and T2-weighted fast spin echo (FSE) images in the same session (repetition time/echo time = 3000/28, 84 milliseconds; NEX = 1; acquisition time = 9 minutes, 54 seconds; matrix = 256 × 256; field of view = 240 mm × 240 mm; slice thickness = 3 mm; no gap; echo train length = 8).

Image Processing and Distortion Correction

During the acquisition of the single-shot echo planar images (EPIs), structural distortion is a serious issue. This acquisition scheme is highly sensitive to susceptibility gradients between brain parenchyma and the surrounding tissues (eg, air, calvarium) as well as to eddy currents induced by large diffusion gradients, resulting in significant spatial distortions. To overcome these problems, we used 2 kinds of image postprocessing techniques. First, we applied distortion correction to diffusion-weighted raw images (b ≠ 0 s/mm^2) based on the T2-weighted EPI (b = 0 s/mm^2)[19,20] on the workstation supplied by the manufacturer (Advantage Workstation 4.0; General Electric Medical Systems). This correction algorithm relies on the maximization of mutual information to estimate the 3 parameters of a geometric distortion model inferred from the acquisition principle. In brief, a residual gradient in the frequency-encoding direction X induces a shear parallel to the phase-encoding direction Y. A residual gradient in Y produces a uniform scaling in the Y direction. A residual gradient in the slice-encoding direction Z produces uniform translation along Y.

The signal intensities of the diffusion-weighted images were then fitted using multivariate linear least-square fitting to obtain the 6 elements of the diffusion tensor on a voxel-by-voxel basis.[1,7] The diffusion tensor was diagonalized to obtain eigenvalues ($\lambda_1>\lambda_2>\lambda_3$) and eigenvectors for each voxel. We used the FA to investigate the warping function that best mapped the EPIs onto the corresponding T2-weighted FSE images, because the FA is a robust intravoxel measure.[3,21] Based on the eigenvalues, the FA was calculated on the voxel-by-voxel basis as follows:

$$\lambda = (\lambda_1 + \lambda_2 + \lambda_3)/3$$

$$FA = \sqrt{3/2} \times \sqrt{[(\lambda_1 - \lambda)^2 + (\lambda_2 - \lambda)^2 + (\lambda_3 - \lambda)^2]} / \sqrt{(\lambda_1^2 + \lambda_2^2 + \lambda_3^2)}$$

Second, distortion-corrected diffusion-weighted EPIs and T2-weighted FSE images as well as FA maps were transferred to a standard personal computer workstation (Dimension 8300, Pentium 4/3GHz; Dell). T2-weighted EPIs were coregistered into T2-weighted FSE images of each subject using an automated image registration program (AIR 5.2.5).[22,23] The functions considered were successive linear (affine 12-parameter model) through sixth-order nonlinear (252-parameter model) 3-dimensional polynomial warping functions. Each warping function was then applied to transform the FA maps to evaluate the effects of spatial warping. We selected 2 regions of interest (ROIs), the genu and splenium of the corpus callosum, because our main purpose in this study was to investigate the topography of the corpus callosum. Spherical ROIs 6 mm in diameter were positioned on the slice of T2-weighted FSE images rather than on the FA maps, in which each anatomic structure was visualized to be of maximal thickness (Fig. 1). After the application of each warping function, the mean and standard deviation (SD) of the FA for each region were measured. Although neuronal fibers in these structures align in a highly coherent manner, resulting in a high FA, they were surrounded by low FA regions (eg, cerebrospinal fluid, gray matter). Therefore, improved registration was determined by increased mean and/or decreased SD of the FA.[24] The statistical significance of difference in the FA mean and SD for order of spatial warping was analyzed by repeated-measures analyses of variance (ANOVA), followed by the post hoc Scheffe test for multiple comparisons. Statistical significance was established at $P < 0.05$.

Diffusion Tensor Tractography

After determining the optimal warping function, the computed transformation parameters were also applied to the distortion-corrected diffusion-weighted EPIs. Diffusion tensor tractography was analyzed with home-built software devel-

Topography of the Human Corpus Callosum Using Diffusion Tensor Tractography

Osamu Abe, MD, DMSc, Yoshitaka Masutani, PhD,* Shigeki Aoki, MD, DMSc,* Hidenori Yamasue, MD,† Haruyasu Yamada, MD,* Kiyoto Kasai, MD,† Harushi Mori, MD,* Naoto Hayashi, MD, DMSc,* Tomohiko Masumoto, MD,* and Kuni Ohtomo, MD, DMSc**

Objective: To evaluate the crossing fiber trajectory through the corpus callosum using distortion-corrected diffusion tensor tractography in the human brain.

Methods: After correcting distortion associated with large-diffusion gradients, T2-weighted echo planar images (EPIs) acquired from 10 right-handed healthy men were coregistered into T2-weighted fast spin echo images using linear through sixth-order nonlinear, 3-dimensional, polynomial warping functions. The optimal transformation parameters were also applied to the distortion-corrected diffusion-weighted EPIs. Diffusion tensor tractography through the corpus callosum was reconstructed, employing the "1 or 2 regions of interest" method.

Results: Compared with the lines through the genu, those through the rostrum ran more inferiorly and seemed to enter the orbital gyrus. Those lines entering posterior temporal white matter (tapetum) crossed through the ventral portion of the splenium and were clearly distinguished from lines that reached parieto-occipital white matter (forceps major).

Conclusion: Diffusion tensor tractography is a feasible noninvasive tool to evaluate commissural fiber trajectory.

Key Words: corpus callosum, brain, anatomy, magnetic resonance imaging, diffusion tensor tractography

(*J Comput Assist Tomogr* 2004;28:533–539)

Diffusion tensor imaging is a newer noninvasive magnetic resonance imaging (MRI) method that provides a means of characterizing the diffusivity of water molecules in the human brain and more pertinent insights into tissue structure, orientation, and temperature not accessible with conventional MRI sequences.[1,2] Diffusion tensor imaging has found application in a wide range of clinical situations such as acute cerebral ischemia, multiple sclerosis, brain maturation, and normal aging.[3–6] It is difficult to visualize the 3-dimensional information of the diffusion tensor into a 2-dimensional imaging plane, however. The means to express diffusion tensor data sets are mean diffusivity, an anisotropy index such as fractional anisotropy (FA),[7] a directionally encoded color map,[8] a vector map, and diffusion tensor tractography (DTT).[9–13] Diffusion tensor tractography reconstructs the 3-dimensional trajectories of white matter tracts, generally by following a continuous path of the greatest diffusivity through the brain from an initial set of seed points. It enables elicitation of white matter connectivity in vivo and is a promising tool to noninvasively elucidate normal neural fiber integrities and those changes in various disease processes.

Diffusion tensor tractography, however, has a few weak points. The first problem is a false-positive line tracking. Water diffuses preferentially along the axis of the fiber bundles, and DTT traces lines depending on the principal axis of the eigenvector associated with the largest eigenvalue of the diffusion tensor. Therefore, DTT does reconstruct lines between the neural fibers, which exist closely and have similar principal axes even when those are not actually interconnected. The second problem is a false-negative line tracking. Because voxel size observed with MRI is much larger than neural fibers, 2 or more white matter fiber bundles with different principal axes intersect within a voxel. As a result, the estimated axis of the first eigenvector is different from the principal axis of each fiber, resulting in early termination or deviation of tracking. Third, there is no gold standard of verifying the accuracy of drawn lines obtained with DTT in individual subjects.

Despite these problems, highly reproducible results in the corpus callosum consistent with those of previous postmortem investigations[15–18] have been shown in the several DTT studies.[10,11,13,14] There is no report to investigate the subdivided topography of the corpus callosum using DTT, however. The purpose of this study is to determine the topographic or-

From the *Department of Radiology, Graduate School of Medicine, University of Tokyo, Tokyo, Japan, and †Department of Neuropsychiatry, Graduate School of Medicine, University of Tokyo, Tokyo, Japan.

Supported in part by a Grant-in-Aid for Scientific Research (C) (2) 15591259 of the Ministry of Education, Science, Sports, and Culture of Japan.

Reprints: Dr Osamu Abe, Department of Radiology, Graduate School of Medicine, University of Tokyo, 7-3-1 Hongo Bunkyo-ku, Tokyo 113-8655, Japan (e-mail: abediag-tky@umin.ac.jp).

ganization of fibers coursing through the human corpus callosum using DTT in comparison with neuroanatomic knowledge.

MATERIALS AND METHODS

Subjects

Diffusion tensor imaging data were acquired from the cranium of 10 right-handed healthy men (24–36 years old, average age: 29.1 ± 4.3 years) without brain morphologic abnormalities, neurologic illness, head trauma, loss of consciousness, or psychiatric disorders. Written informed consent was obtained from all subjects according to the Declaration of Helsinki, and the scanning protocol was approved by the local ethical committee at our institution.

MRI Acquisition Protocol

All scans were acquired on a 1.5-T Signa Echo Speed MRI system (General Electric Medical Systems, Milwaukee, WI). A circularly polarized head coil was used for radiofrequency transmission and reception of the nuclear magnetic resonance signal. The pulse sequence we used in this study was single-shot, diffusion-weighted, echo planar acquisition (repetition time/echo time = 6000/78.2 milliseconds; numbers of excitation (NEX) = 4; acquisition time = 5 minutes, 36 seconds; matrix = 128 × 128; field of view = 240 mm × 240 mm; slice thickness = 5 mm; no gap; b value = 1000 s/mm^2; diffusion gradient directions = [0, 0, 0], [$1/\sqrt{2}$, 0, $1/\sqrt{2}$], [$-1/\sqrt{2}$, 0, $1/\sqrt{2}$], [0, $1/\sqrt{2}$, $1/\sqrt{2}$], [0, $1/\sqrt{2}$, $-1/\sqrt{2}$], [$1/\sqrt{2}$, $1/\sqrt{2}$, 0], and [$-1/\sqrt{2}$, $1/\sqrt{2}$, 0]). We also acquired proton density–weighted and T2-weighted fast spin echo (FSE) images in the same session (repetition time/echo time = 3000/28, 84 milliseconds; NEX = 1; acquisition time = 9 minutes, 54 seconds; matrix = 256 × 256; field of view = 240 mm × 240 mm; slice thickness = 3 mm; no gap; echo train length = 8).

Image Processing and Distortion Correction

During the acquisition of the single-shot echo planar images (EPIs), structural distortion is a serious issue. This acquisition scheme is highly sensitive to susceptibility gradients between brain parenchyma and the surrounding tissues (eg, air, calvarium) as well as to eddy currents induced by large diffusion gradients, resulting in significant spatial distortions. To overcome these problems, we used 2 kinds of image postprocessing techniques. First, we applied distortion correction to diffusion-weighted raw images (b ≠ 0 s/mm^2) based on the T2-weighted EPI (b = 0 s/mm^2)[19,20] on the workstation supplied by the manufacturer (Advantage Workstation 4.0; General Electric Medical Systems). This correction algorithm relies on the maximization of mutual information to estimate the 3 parameters of a geometric distortion model inferred from the acquisition principle. In brief, a residual gradient in the frequency-encoding direction X induces a shear parallel to the phase-encoding direction Y. A residual gradient in Y produces a uniform scaling in the Y direction. A residual gradient in the slice-encoding direction Z produces uniform translation along Y.

The signal intensities of the diffusion-weighted images were then fitted using multivariate linear least-square fitting to obtain the 6 elements of the diffusion tensor on a voxel-by-voxel basis.[1,7] The diffusion tensor was diagonalized to obtain eigenvalues ($\lambda_1 > \lambda_2 > \lambda_3$) and eigenvectors for each voxel. We used the FA to investigate the warping function that best mapped the EPIs onto the corresponding T2-weighted FSE images, because the FA is a robust intravoxel measure.[3,21] Based on the eigenvalues, the FA was calculated on the voxel-by-voxel basis as follows:

$$\lambda = (\lambda_1 + \lambda_2 + \lambda_3)/3$$

$$FA = \sqrt{3/2} \times \sqrt{[(\lambda_1 - \lambda)^2 + (\lambda_2 - \lambda)^2 + (\lambda_3 - \lambda)^2]} / \sqrt{(\lambda_1^2 + \lambda_2^2 + \lambda_3^2)}$$

Second, distortion-corrected diffusion-weighted EPIs and T2-weighted FSE images as well as FA maps were transferred to a standard personal computer workstation (Dimension 8300, Pentium 4/3GHz; Dell). T2-weighted EPIs were coregistered into T2-weighted FSE images of each subject using an automated image registration program (AIR 5.2.5).[22,23] The functions considered were successive linear (affine 12-parameter model) through sixth-order nonlinear (252-parameter model) 3-dimensional polynomial warping functions. Each warping function was then applied to transform the FA maps to evaluate the effects of spatial warping. We selected 2 regions of interest (ROIs), the genu and splenium of the corpus callosum, because our main purpose in this study was to investigate the topography of the corpus callosum. Spherical ROIs 6 mm in diameter were positioned on the slice of T2-weighted FSE images rather than on the FA maps, in which each anatomic structure was visualized to be of maximal thickness (Fig. 1). After the application of each warping function, the mean and standard deviation (SD) of the FA for each region were measured. Although neuronal fibers in these structures align in a highly coherent manner, resulting in a high FA, they were surrounded by low FA regions (eg, cerebrospinal fluid, gray matter). Therefore, improved registration was determined by increased mean and/or decreased SD of the FA.[24] The statistical significance of difference in the FA mean and SD for order of spatial warping was analyzed by repeated-measures analyses of variance (ANOVA), followed by the post hoc Scheffe test for multiple comparisons. Statistical significance was established at $P < 0.05$.

Diffusion Tensor Tractography

After determining the optimal warping function, the computed transformation parameters were also applied to the distortion-corrected diffusion-weighted EPIs. Diffusion tensor tractography was analyzed with home-built software devel-

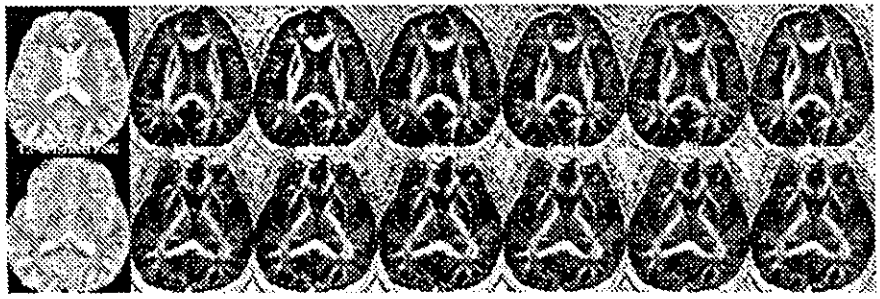

FIGURE 1. Regions of interest (ROIs) in the genu and splenium of the corpus callosum. Spherical ROIs (shown in white) 6 mm in diameter were positioned on the slice of T2-weighted fast spin echo images (genu: upper left, splenium: lower left) rather than on fractional anisotropy (FA) maps, in which each anatomic structure was visualized to be of maximal thickness. The ROIs were also overlaid on spatially warped FA maps.

oped by 1 of the authors (Y.M.).[25] This software is available on the web (http://www.ut-radiology.umin.jp/people/masutani/dTV_frame-e.htm). The eigenvector associated with the largest eigenvalue or the principal axis was assumed to represent the local fiber direction. A set of locations for the initiation of the tracking algorithm or "seed-volumes" was first selected on reconstructed midsagittal T2-weighted images. The tracking algorithm then moved a distance of 0.66 mm along the principal axis. The diffusion tensor at the next location was determined from the adjacent voxels by trilinear filtering, and its principal axis was subsequently estimated. The tracking then traveled a further 0.66 mm along this direction. Tracking lines were traced in this way and were propagated in antegrade and retrograde directions until the FA fell below an assigned threshold (FA = 0.2).

Seed-volumes were located on the dorsal and ventral halves of the genu and the rostrum. The body and the splenium of the corpus callosum were composed of neural fibers that run closely to each other but are destined to different targets, however. To separate these fibers, the "2 regions of interest" method was used as described in previous articles.[9,25,26] This method was used to define the second ROI or target volume that exclusively contained fibers of interest at a certain distance from the seed-volume. Freehand-drawn ROIs were set as starting points in the areas, including the body and splenium of the corpus callosum, and tracking lines were retained if those lines entered target volumes. Target volumes were located lateral or superior to the body at temporal or parieto-occipital white matter, respectively, in terms of the tracking in the splenium. Typical computation time to reconstruct trajectories per analysis was 5–10 seconds running on a standard personal computer workstation (Dimension 8300).

RESULTS

Optimal Order of Spatial Warping Function

For the genu, repeated-measures ANOVA revealed statistical differences in the mean ($P < 0.0001$) and SD ($P < 0.0001$) between groups. The Scheffe test showed that there were significant increases in the mean with the fourth-order ($P = 0.0085$), fifth-order ($P = 0.0005$), and sixth-order ($P = 0.0007$) spatial warps compared with the second-order warps and that there was no other significant change in the mean (Fig. 2A). The post hoc test showed that there were significant decreases in the SD with the fifth-order and sixth-order spatial

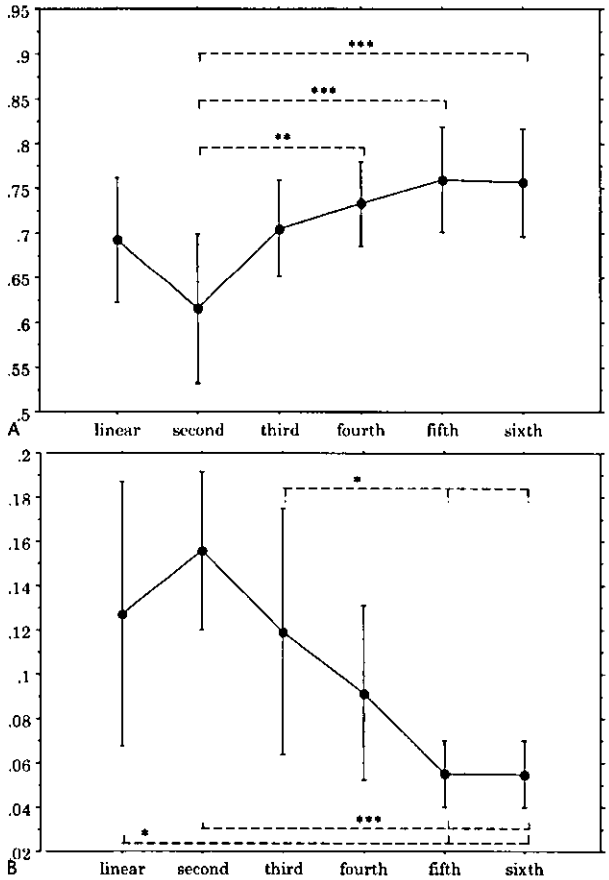

FIGURE 2. The mean and standard deviation for the fractional anisotropy in the genu after linear through sixth-order spatial warping. *$P < 0.05$, **$P < 0.01$, and ***$P < 0.001$ indicates statistical significance with the post hoc Scheffe test. The data are expressed as mean ± SD.

warps compared with the linear-order ($P = 0.015$ for fifth-order, $P = 0.014$ for sixth order), second-order ($P = 0.0001$ for fifth-order and sixth-order), and third-order ($P = 0.043$ for fifth-order, $P = 0.042$ for sixth-order) warps (see Fig. 2B). In contrast, for the splenium, repeated-measures ANOVA revealed no significant change between groups (Fig. 3). Thus, we concluded that the fifth-order polynomial warping function provided the optimal distortion-correction scheme to investigate the topography of the corpus callosum.

Diffusion Tensor Tractography

The tracking lines (forceps minor) crossing through the ventral half of the genu commonly passed along the medial course to the frontal lobe, and those through the dorsal half passed along the lateral course (Fig. 4). In contrast, the lines crossing through the rostrum of the corpus callosum ran along the more inferior course and seemed to go into the orbital surfaces of the frontal lobes. The tracking lines through the body mainly passed along the upper course to the frontal or parietal lobe (Fig. 5). A smaller number of lines ran along the lateral

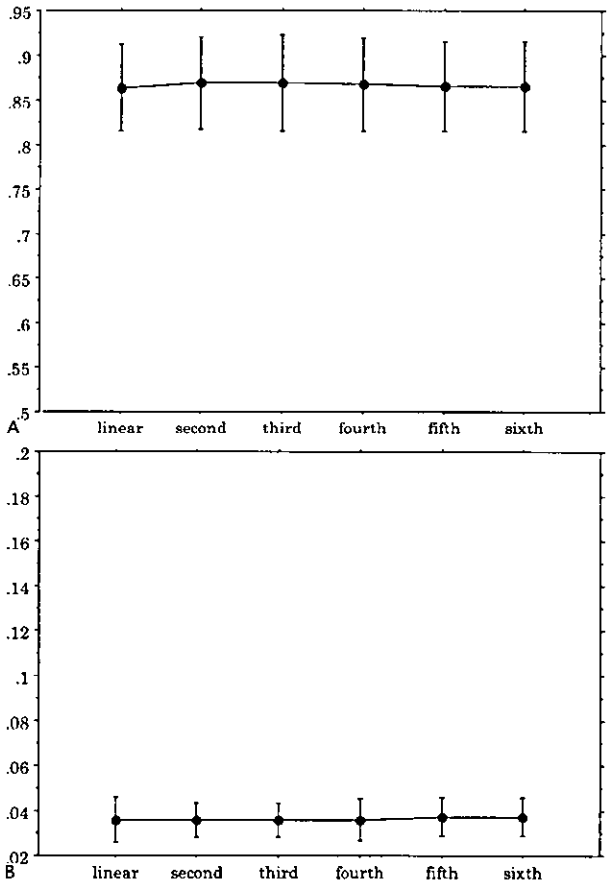

FIGURE 3. The mean and standard deviation for the fractional anisotropy in the splenium after linear through sixth-order spatial warping. No statistical significant differences were revealed with repeated-measures ANOVA. The data are expressed as mean ± SD.

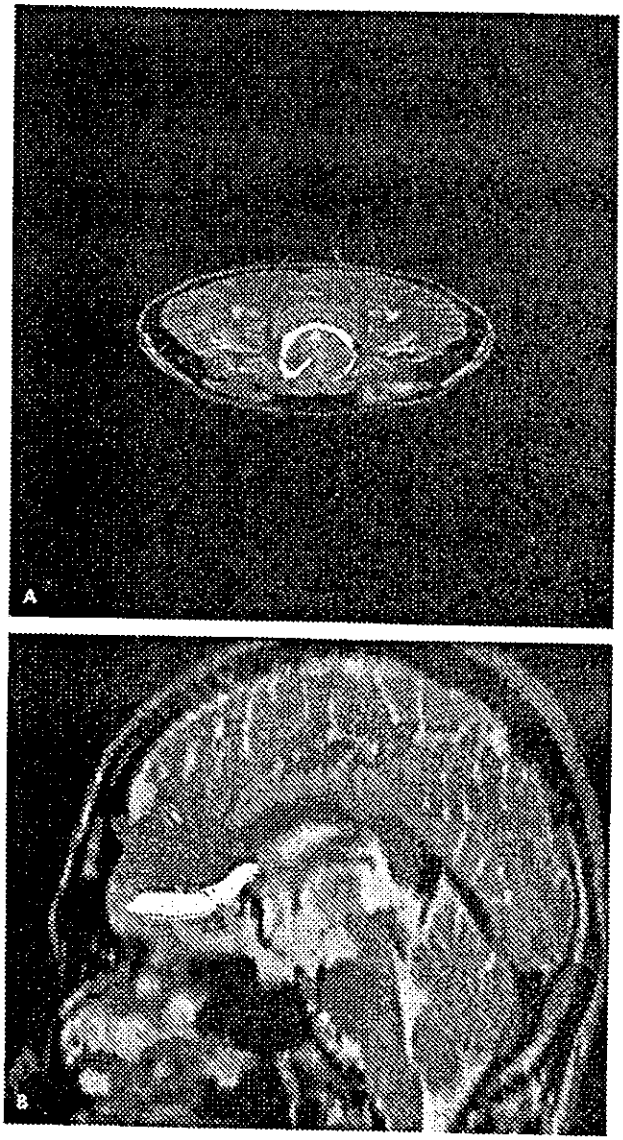

FIGURE 4. Diffusion tensor tractography through the genu and the rostrum of the corpus callosum. The frontal (A) and lateral (B) views are overlaid on axial and sagittal T2-weighted fast spin echo images, respectively. The tracking lines crossing through the ventral half of the genu (shown in red) commonly passed along the medial course to frontal lobe, and those through the dorsal half (shown in blue) passed along the lateral course. The lines crossing through the rostrum (shown in yellow) ran along the more inferior course compared with the forceps minor and seemed to go into the orbital surfaces of the frontal lobes.

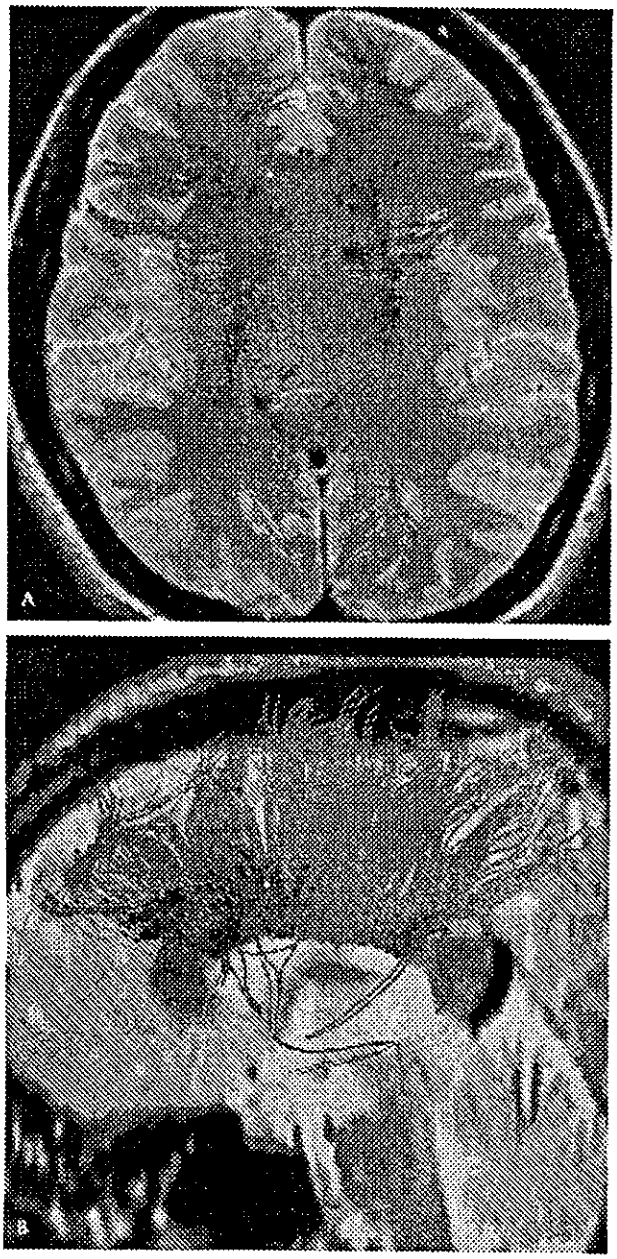

FIGURE 5. Diffusion tensor tractography through the body of the corpus callosum. The superoinferior (A) and lateral (B) views are overlaid on axial and sagittal T2-weighted fast spin echo images, respectively. The tracking lines through the body mainly passed along the upper course to the frontal or parietal lobe (shown in red). A smaller number of lines (shown in blue) ran along the lateral course, probably because of partial volume averaging in the corona radiata or semiovale center, where white matter tracts with a wide variety of directions were intermingled (eg, superior longitudinal fasciculus).

course, probably because of partial volume averaging in the corona radiata or semiovale center, where white matter tracts with a wide variety of directions were intermingled (eg, superior longitudinal fasciculus). The tracking lines that entered posterior temporal white matter (tapetum) crossed through the ventral portion of the splenium. In the splenium of the corpus callosum, the lines representing the tapetum were surrounded by the lines that reached parieto-occipital white matter (forceps major) and were clearly distinguished (Fig. 6). These results were consistent in all subjects, and there was no exceptional case.

DISCUSSION

We have shown the crossing fiber trajectories through the corpus callosum with distortion-corrected DTT. The neuroanatomic investigations have shown that the corpus callosum consists of 4 parts.[15–18] The genu of the corpus callosum connects the lateral and medial surfaces of the frontal lobes, forming the forceps minor. The rostrum of the corpus callosum is the thin ventral tapering portion extending from the genu to the lamina terminalis, connecting the orbital surfaces of the frontal lobes. The body of the corpus callosum extends between the genu and the splenium, connecting wide neocortical homotopic regions of the cerebral hemispheres. Our DTT results in these regions were concordant with those of previous neuroanatomic studies.[15–18] Unlike postmortem studies, however, DTT is completely noninvasive in nature, and it is possible to sequentially compare in vivo alterations in tracking results in normal maturation and aging as well as in patients with various disorders affecting the corpus callosum.

The most intriguing finding is that the trajectories destined to temporal and parieto-occipital white matter (these fibers are referred to as the tapetum and forceps major, respectively) were clearly separated in the splenium of the corpus callosum. The neuroanatomic studies have revealed some fibers from the splenium of the corpus callosum that cover the roofs of the lateral ventricle, further extending to cover the lateral aspect of the temporal horns of the lateral ventricles on each side, thereby forming the tapetum.[17,18] To our knowledge, however, no neuroanatomic description has reported what portion of the corpus callosum the fiber bundles that go into the tapetum or forceps major pass through. Although the problem caused by 2 or more crossing fibers within a voxel, as described previously in this report, might obscure a few tracking lines that intersect in the corpus callosum, we believe that most fiber bundles destined to go into the tapetum and forceps major exist separately in the corpus callosum. This finding is to be elucidated in the future, but if this is the case, the disruption of the fiber bundles originating from the tapetum and the forceps major may occur asynchronously and should be evaluated separately. In such a situation, DTT may help to determine the position of the ROI.

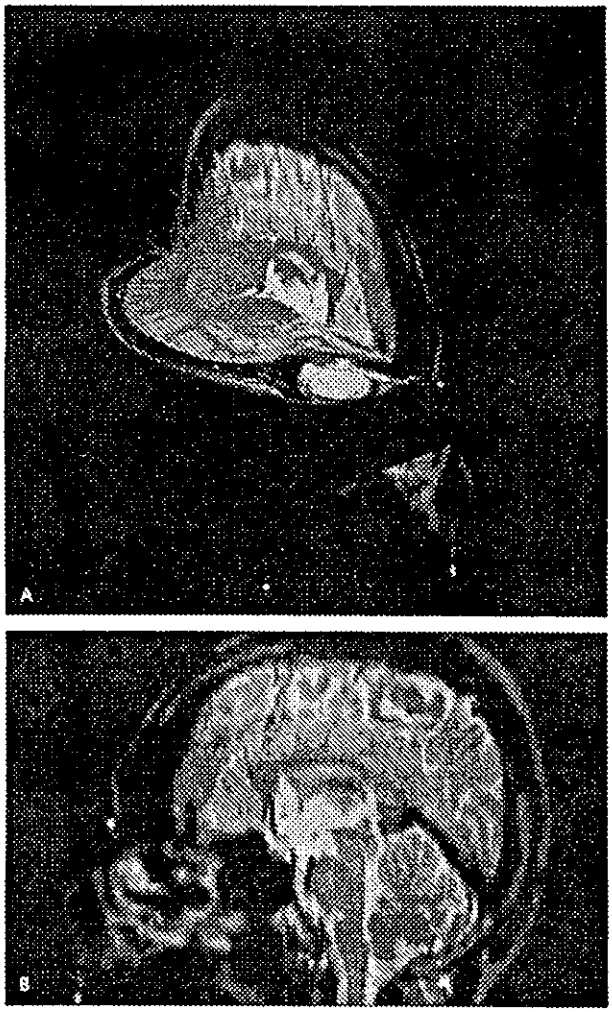

FIGURE 6. Diffusion tensor tractography through the caudal portion of the body and splenium of the corpus callosum. A, Three-dimensional projections of the tracking lines overlaid on axial and sagittal T2-weighted fast spin echo images. The lines that entered posterior temporal white matter (tapetum) crossed through the ventral portion of the splenium of the corpus callosum (shown in red). B, In-plane location overlaid on a sagittal T2-weighted fast spin echo image. In the splenium of the corpus callosum, the lines representing the tapetum were surrounded by the lines that reached parieto-occipital white matter (forceps major, shown in blue) and were clearly distinguished.

There are a few limitations to this study. First, the nominal spatial resolution is 1.9 mm × 1.9 mm × 5 mm, which is larger than the size of the neural fibers, ranging from 10 to 100 μm. Even if the slice thickness is 2.5–3 mm, each voxel measured with MRI or DTT contains a large number of neural fibers with different principal axes that intersect within a voxel. As a result, when the principal axis of each fiber is not oriented in a highly coherent manner, the estimated axis of the first eigenvector is different from the actual direction of each fiber, resulting in early termination or deviation of tracking. Furthermore, the normal subjects we investigated in this study were enrolled in the ongoing cohort study of patients with psychiatric disorders, and it was necessary to share the scanning protocol in the normal volunteers and patients. Some patients may be sensitive to nerve-racking noise during EPI acquisition, and longer acquisition time is not likely to be feasible in the clinical setting.

The second limitation rests in how to determine the normal and pathologic variations in patterns of the reconstructed fiber lines and their association with different cortical areas. It is important to establish the procedures to reconstruct the fiber trajectories in different human subjects reproducibly and to validate them qualitatively through comparison with neuroanatomic results, as in this study. Nevertheless, it can be hard to assess the interindividual variability of these reconstructed axonal tracts in the individual's frame of reference. Recently, spatially normalized diffusion tensor data have been presented for analyzing the spatial distribution of neural fibers in the brain and enabled to evaluate the interindividual variability in a common spatial reference frame (Talairach space).[11–13] Although this is a promising methodology to elucidate changes in fiber integrity and connectivity during pathologic processes, spatial normalization may obscure subtle interindividual variation. The aim of our study is to clarify the crossing fiber trajectory through the corpus callosum, and spatial normalization is beyond the scope of this study. It is an issue in our ongoing research, however.

In summary, notwithstanding a few limitations, DTT is a feasible noninvasive tool to evaluate the commissural fiber trajectory, especially in the rostrum, genu, and splenium of the corpus callosum, where these results were concordant with the classic descriptions of postmortem neuroanatomic studies. The preliminary normative data presented here will contribute to evaluations of the functional or morphologic impairments of the corpus callosum.

ACKNOWLEDGMENT

The authors thank Hiroyuki Kabasawa (General Electric Yokogawa Medical Systems, Tokyo, Japan) for technical assistance.

REFERENCES

1. Basser PJ, Mattiello J, LeBihan D. MR diffusion tensor spectroscopy and imaging. *Biophys J.* 1994;66:259–267.
2. Pierpaoli C, Jezzard P, Basser PJ, et al. Diffusion tensor MR imaging of the human brain. *Radiology.* 1996;201:637–648.
3. Sorensen AG, Wu O, Copen WA, et al. Human acute cerebral ischemia: detection of changes in water diffusion anisotropy by using MR imaging. *Radiology.* 1999;212:785–792.

4. Werring DJ, Brassat D, Droogan AG, et al. The pathogenesis of lesions and normal-appearing white matter changes in multiple sclerosis: a serial diffusion MRI study. *Brain*. 2000;123:1667–1676.
5. Huppi PS, Maier SE, Peled S, et al. Microstructural development of human newborn cerebral white matter assessed in vivo by diffusion tensor magnetic resonance imaging. *Pediatr Res*. 1998;44:584–590.
6. Abe O, Aoki S, Hayashi N, et al. Normal aging in the central nervous system: quantitative MR diffusion-tensor analysis. *Neurobiol Aging*. 2002;23:433–441.
7. Basser PJ. Inferring microstructural features and the physiological state of tissues from diffusion-weighted images. *NMR Biomed*. 1995;8:333–344.
8. Pajevic S, Pierpaoli C. Color schemes to represent the orientation of anisotropic tissues from diffusion tensor data: application to white matter fiber tract mapping in the human brain. *Magn Reson Med*. 1999;42:526–540.
9. Conturo TE, Lori NF, Cull TS, et al. Tracking neuronal fiber pathways in the living human brain. *Proc Natl Acad Sci USA*. 1999;96:10422–10427.
10. Mori S, Kaufmann WE, Pearlson GD, et al. In vivo visualization of human neural pathways by magnetic resonance imaging. *Ann Neurol*. 2000;47:412–414.
11. Mori S, Kaufmann WE, Davatzikos C, et al. Imaging cortical association tracts in the human brain using diffusion-tensor-based axonal tracking. *Magn Reson Med*. 2002;47:215–223.
12. Xu D, Mori S, Solaiyappan M, et al. A framework for callosal fiber distribution analysis. *Neuroimage*. 2002;17:1131–1143.
13. Jones DK, Griffin LD, Alexander DC, et al. Spatial normalization and averaging of diffusion tensor MRI data sets. *Neuroimage*. 2002;17:592–617.
14. Poupon C, Clark CA, Frouin V, et al. Regularization of diffusion-based direction maps for the tracking of brain white matter fascicles. *Neuroimage*. 2000;12:184–195.
15. de Lacoste MC, Kirkpatrick JB, Ross ED. Topography of the human corpus callosum. *J Neuropathol Exp Neurol*. 1985;44:578–591.
16. Nieuwenhuys R, Voogd J, van Huijzen C. *The Human Central Nervous System*. Berlin: Springer Verlag; 1988.
17. Jinkins J. *Atlas of Neuroradiologic Embryology, Anatomy, and Variants*. Philadelphia: Lippincott Williams & Wilkins; 2000.
18. Crosby E, Humphrey T, Lauer E. *Correlative Anatomy of the Nervous System*. New York: Macmillan; 1962.
19. Haselgrove JC, Moore JR. Correction for distortion of echo-planar images used to calculate the apparent diffusion coefficient. *Magn Reson Med*. 1996;36:960–964.
20. Mangin J, Poupon C, Clark C, et al. Eddy-current distortion correction and robust tensor estimation for MR diffusion imaging. *Medical Image Computing and Computer-Assisted Intervention (MICCAI)*. 2001; LNCS2208:186–194.
21. Papadakis NG, Xing D, Houston GC, et al. A study of rotationally invariant and symmetric indices of diffusion anisotropy. *Magn Reson Imaging*. 1999;17:881–892.
22. Woods RP, Grafton ST, Watson JD, et al. Automated image registration: II. Intersubject validation of linear and nonlinear models. *J Comput Assist Tomogr*. 1998;22:153–165.
23. Woods RP, Grafton ST, Holmes CJ, et al. Automated image registration: I. General methods and intrasubject, intramodality validation. *J Comput Assist Tomogr*. 1998;22:139–152.
24. Pfefferbaum A, Sullivan EV, Hedehus M, et al. Age-related decline in brain white matter anisotropy measured with spatially corrected echo-planar diffusion tensor imaging. *Magn Reson Med*. 2000;44:259–268.
25. Masutani Y, Aoki S, Abe O, et al. MR diffusion tensor imaging: recent advance and new techniques for diffusion tensor visualization. *Eur J Radiol*. 2003;46:53–66.
26. Catani M, Howard RJ, Pajevic S, et al. Virtual in vivo interactive dissection of white matter fasciculi in the human brain. *Neuroimage*. 2002;17:77–94.

ELSEVIER

International Journal of Psychophysiology 45 (2002) 211–225

INTERNATIONAL JOURNAL OF PSYCHOPHYSIOLOGY

www.elsevier.com/locate/ijpsycho

Psychophysiological index during auditory selective attention correlates with visual continuous performance test sensitivity in normal adults

Kiyoto Kasai[a], Kazuyuki Nakagome[b,*], Ken-Ichi Hiramatsu[c], Masato Fukuda[d], Makoto Honda[e], Akira Iwanami[f]

[a]*Department of Psychiatry, Harvard Medical School, Brockton VA Medical Center, Department of Psychiatry-116A, 940 Belmont Street Brockton, Boston, MA 02301, USA*

[b]*Department of Psychiatry, Showa University School of Medicine, 1-5-8 Hatanodai, Shinagawa-ku, Tokyo 142-8566, Japan*

[c]*Department of Neuropsychiatry, School of Medicine, University of the Ryukyus, 207, Aza Uehara, Nishihara-cho, Nakagami-gun, Okinawa, 903-0215, Japan*

[d]*Department of Neuropsychiatry, Gunma University School of Medicine, 3-39-15 Showa-machi, Maebashi, Gunma, 371-8511, Japan*

[e]*Center for Narcolepsy, Department of Psychiatry and Behavioral Sciences, Stanford University School of Medicine, 701-B Welch Road, Rm 116, MC: 5742, Palo Alto, CA 94304, USA*

[f]*Department of Neuropsychiatry, Graduate School of Medicine, University of Tokyo, 7-3-1 Hongo, Bunkyo-ku, Tokyo, 113-8655, Japan*

Received 1 February 2002; received in revised form 26 February 2002; accepted 26 February 2002

Abstract

The continuous performance test (CPT) provides a reliable index of cognitive function, but it is still unclear what aspects of processing this test measures. This study aimed to investigate the contribution of different aspects of cognitive function to the performance on degraded stimulus CPT (DSCPT), which requires a higher level of mental effort than the conventional CPT. Event-related potential (ERP) components, MMN, N2b, and early and late Nds were measured at 16 electrode sites in 19 right-handed normal volunteers using an auditory selective attention task. The association between CPT sensitivity ratings (sensitivity A′) and amplitudes of each component was examined for each electrode site. The CPT sensitivity A′ showed a significant positive correlation with the N2b amplitude in the fronto-central and temporal regions, predominantly in the right hemisphere and specifically to the right ear of stimulation. This finding suggests that the controlled deviance detection process was related to DSCPT performance.

Keywords: Mismatch negativity; N2b; Nd; Event-related potentials; Selective attention task; Continuous performance test (CPT)

*Corresponding author. Tel.: +81-3-3784-8703; fax: +81-3-3784-8703.
E-mail address: nakagome@med.showa-u.ac.jp (K. Nakagome).

0167-8760/02/$ - see front matter
PII: S0167-8760(02)00013-2

1. Introduction

The Continuous Performance Test (CPT) was originally designed to detect deficits in sustained attention among brain-damaged patients and has been modified to be widely used in studies of psychiatric diseases (Walker, 1981; Nuechterlein, 1983; O'Dougherty et al., 1984; Cornblatt et al., 1989), such as schizophrenia (Rutschmann et al., 1977; Nuechterlein, 1983; Cornblatt and Erlenmeyer-Kimling, 1985; Nuechterlein et al., 1991). During the task, subjects are presented with single letters or numbers in a short duration that appear at a rapid fixed rate. The subjects are required to respond with a button press each time a predesignated target stimulus appears. A variation of the task uses perceptually degraded stimuli (DSCPT), which requires a high level of mental effort in perception. The DSCPT has been reported to measure early stages of visual information processing (Nuechterlein and Dawson, 1984). Nuechterlein et al. (1991) also suggested that the DSCPT showed a deteriorated signal/noise discrimination sensitivity in schizophrenic patients similarly during the psychotic and the remitted stages, indicating that the target detection sensitivity of the DSCPT might be a stable vulnerability indicator of schizophrenia. Accordingly, DSCPT was adopted in this study, due to our interest in the search for objective indicators of schizophrenic vulnerability, which is relevant to the field of clinical psychiatry.

One of the psychometric properties of the CPT is that the task is intended to measure vigilance and/or perceptual performance, as well as sustained attention over time (Cornblatt et al., 1989). However, although the test shows marked sensitivity in discerning psychiatric populations from normal control subjects, as noted above, its construct validity has not been well established. Even automatic stimulus perceptual capacity, independent from attention, may also contribute to the CPT performance. Unless the construct validity is established, the implications obtained from the test might be obscured. In an attempt to elucidate this controversy, in addition to DSCPT measurement, event-related potentials (ERPs) were measured in normal subjects using an auditory selective attention task, in which each stage of processing can be estimated from several distinct ERP components. An auditory, but not visual, selective task was adopted, because mismatch negativity (MMN), presumably reflecting automatic processing, has been consistently reported using an auditory modality. Although controversy in the interpretation of these ERP components remains, the relation between these ERP indices and CPT performance level should contribute to our further understanding in terms of what aspect of processing mainly determines the CPT performance level.

A selective attention task enabled us to investigate Nd, MMN and N2b, which have been shown to reflect different aspects of stimulus processing in an identical state of focused attention. A selective attention task required the subjects to focus on one ear and silently count the deviant stimuli, which differed in stimulus duration from the standard stimuli, while ignoring all the stimuli delivered to the contralateral ear. Either of the components was obtained in the difference waveforms between either two of the ERPs elicited by four distinct stimulus types (attended/unattended, deviant/standard).

First, Nds represent focused attention, which were obtained by subtracting the ERPs to the standard stimuli in the unattended condition from those in the attended condition. Previous studies suggested two separate negativities differing in their latency and scalp distribution (Hansen and Hillyard, 1980, 1984; Okita et al., 1983). The early component (Nde), showing a fronto-centrally dominant distribution, was suggested to reflect focused attention, whereas the late component (Ndl) shows a more anteriorly shifted distribution than the Nde and, although speculative, it is related to the attentional supervisory system, which mediates the selective rehearsal and maintenance of the attentional trace (Näätänen, 1982). Second, MMN reflects automatic deviance detection processing (Näätänen et al., 1982; Näätänen, 1992), which were obtained by subtracting the ERPs to the frequent stimuli from the rare stimuli in the unattended condition. Finally, N2b was suggested to reflect controlled deviance detection processing (Ritter et al., 1979, 1988; Novak et al., 1990). An important implication concerning the N2b is that

the amplitude was measured in the difference waveform obtained by subtracting the ERPs to the standard stimuli from those to the deviant stimuli in the attended condition, because the N2b measured from the difference waveform should be less contaminated with other ERP components, such as P2 or Nd, the effect of which is presumably removed by the subtraction (O'Donnell et al., 1993).

It is noted, however, that these interpretations of the ERP components remain controversial, as indicated by findings suggesting an incremental effect of attention on MMN amplitude (Woldorff et al., 1991; Oades and Dittmann-Balcar, 1995; Trejo et al., 1995), which contradicts the above view that MMN reflects automatic processing.

The present report is part of a study conducted in 1997, from which the ERP findings (MMN and N2b) of the schizophrenic patients and normal control subjects were previously reported (Kasai et al., 1999). In our previous publication, we reported a significant amplitude reduction of MMN and N2b in schizophrenic patients compared with the normal control subjects. Furthermore, significant attentional effects on MMN amplitude and its distribution were not detected and contralateral predominance of MMN and N2b was suggested, although the hemispheric difference in MMN was significant only when elicited by left ear stimulation. It was thus suggested that the processing stages reflected by these components are mainly mediated in the contralateral hemisphere to the stimulated ear. These findings are in line with a few previous observations, which suggested a contralateral predominance of MMN (Giard et al., 1990; Woods, 1992; Deouell et al., 1998) and N2b (Woods, 1992; Woods et al., 1992) with regard to ear of stimulation. Therefore, it might be assumed that each hemispheric activity can be separately tapped for these indices elicited by each stimulated ear, which is one of the merits of the selective attention task adopted in this study.

2. Methods

2.1. Subjects

A total of 19 healthy young subjects (10 male and 9 female; mean age=25.3, S.D.=5.3 years) participated in the study. The subjects gave written informed consent for their participation. All subjects were right-handed with normal hearing and visual acuity, and had no history of psychiatric illness, severe head injury or substance use disorders.

2.2. CPT procedure and measurement

The computerized version of the degraded-stimulus version of the continuous performance task (DSCPT; provided by Nuechterlein, 1983) was administered to all subjects. DSCPT randomly presents on a computer screen perceptually degraded single-digit numbers between 0 and 9 for 33 ms each, at a rate of 1/s. The stimuli were presented with background visual noise: black/white reversal of a random 40% of pixels was used to produce degradation. Subjects, with their eyes positioned 1 m from the computer screen, were required to respond to the target stimulus, the number '0', by pressing a button. A total of 480 trials, 25% of them targets, were divided into six consecutive blocks presented over 8 min.

Probabilities of hits and false alarms were used to calculate a non-parametric signal detection index of sensitivity (CPT sensitivity A') for the CPT (Grier, 1971). The term sensitivity refers to the signal/noise discrimination level. Overall CPT sensitivity A' was calculated by averaging the means from the six consecutive 80-trial blocks.

2.3. ERP task and recording

The subjects performed an auditory selective attention task after finishing DSCPT. During the task, tone pips of 1 kHz, 70 dB SPL (rise/fall time of 10 ms) were presented dichotically to the subjects' ears via headphones. The whole task involved six blocks of tone pips. Each block consisted of 50 deviant stimuli (probability 25%) and 150 standard stimuli (75%), varying in duration, presented to each ear in random order. The duration of the deviant stimuli was 50 ms and that of the standard stimuli was 100 ms. The interstimulus interval was fixed at 600 ms. The subjects were required to focus on one ear and silently count the deviant stimuli while ignoring all the

stimuli delivered to the contralateral ear. Ear designation was counterbalanced across the blocks. In addition, the order of ear designation through the sequential blocks was counterbalanced across the subjects.

While performing the task, the subjects sat comfortably in a dimly lit, soundproof, electrically shielded room. EEGs were recorded via 16 Ag–AgCl electrodes placed according to the international 10–20 system at Fp1, Fp2, F3, Fz, F4, T3, C3, Cz, C4, T4, T5, P3, Pz, P4, T6 and Oz. The tip of the nose was used as a reference for all the electrodes. Two electrodes were placed at the outer canthus and above the left eye to monitor eye movements. The sampling rate was 500 Hz/channel, and the analog filter bandpass was 0.16–60 Hz. The analysis period was 512 ms, including a 64-ms prestimulus baseline. Averaging and artifact rejection were conducted on-line with a DP-1100 (NEC, Japan). The baseline was separately corrected for each channel according to the mean amplitude of the EEG over 64 ms prior to stimulus onset. The EEG epochs that contained peak-to-peak amplitudes exceeding 150 μV at any electrode were automatically excluded from averaging. The average waveforms were separately obtained for deviant and standard stimuli for each ear, and digitally filtered with a cut-off frequency of 30 Hz.

MMN/N2b were measured in the difference ERPs obtained by subtracting ERPs of standard stimuli from those of deviant stimuli separately for each ear of stimulation in the unattended and attended conditions. Nd was measured in the difference ERPs of the standard stimuli obtained by subtracting ERPs in the unattended condition from those in the attended condition. MMN, N2b and early and late Nds were scored as the mean amplitudes in the time windows of 120–200, 240–320, 160–240 and 280–360 ms. The time windows for measuring ERP mean amplitudes were estimated from the grand-average difference waveforms. Counting performance was assessed by determining the average rate of deviation of the counts from the current number of targets for each ear of stimulation.

2.4. Statistical analysis

For assessment of the temporal nature and gender difference in CPT performance, a repeated-measures analysis of variance (ANOVA) was performed on each index in each block, with gender representing the inter-individual factor and block representing the intra-individual factor. ERP findings were analyzed to elucidate the topographical feature of each component using the repeated-measures ANOVA on the vector-normalized data, according to the method of McCarthy and Wood (1985), with ear of stimulation and selected electrode sites as intra-individual factors. The electrode sites were selected from the grand-averaged difference waveforms, where negative deflections were clearly observed within the time window of amplitude measurement. Degrees of freedom were reduced using the Greenhouse–Geisser correction. Spearman rank correlation coefficients were calculated between overall non-parametric CPT sensitivity A′ and the ERP indices for each electrode position. Moreover, correlations between the counting performance in the ERP task and CPT sensitivity A′ ERP indices in each electrode position were also tested.

3. Results

3.1. CPT performance

The CPT performance indices are summarized in Table 1. Neither of the overall indices showed a significant correlation with age. The hit rate and false alarm rate both showed a decrement over blocks, resulting in a small decrement in the sensitivity A′, but the effect of blocks failed to reach the significance level for either index.

3.2. ERP indices

The mean error rates in reporting the number of deviants were not significantly different between the ear of stimulation, which were 10.2% for the left ear tones and 9.4% for the right ear tones. The difference ERPs to attended tones were characterized by the P3 component that was not evident for

Table 1
CPT performance indices

	Block 1	Block 2	Block 3	Block 4	Block 5	Block 6	Total
Hit rate (%)	80.8 (21.4)	80.8 (20.8)	75.0 (27.1)	73.4 (27.2)	74.2 (25.9)	71.6 (18.9)	75.8 (18.9)
False alarm rate (%)	6.5 (5.6)	6.4 (5.7)	5.4 (5.7)	5.6 (5.7)	5.1 (4.0)	5.3 (4.8)	5.7 (4.4)
Sensitivity A'	0.913 (0.114)	0.916 (0.105)	0.909 (0.080)	0.898 (0.084)	0.903 (0.109)	0.905 (0.057)	0.915 (0.063)

Values are mean (S.D.).

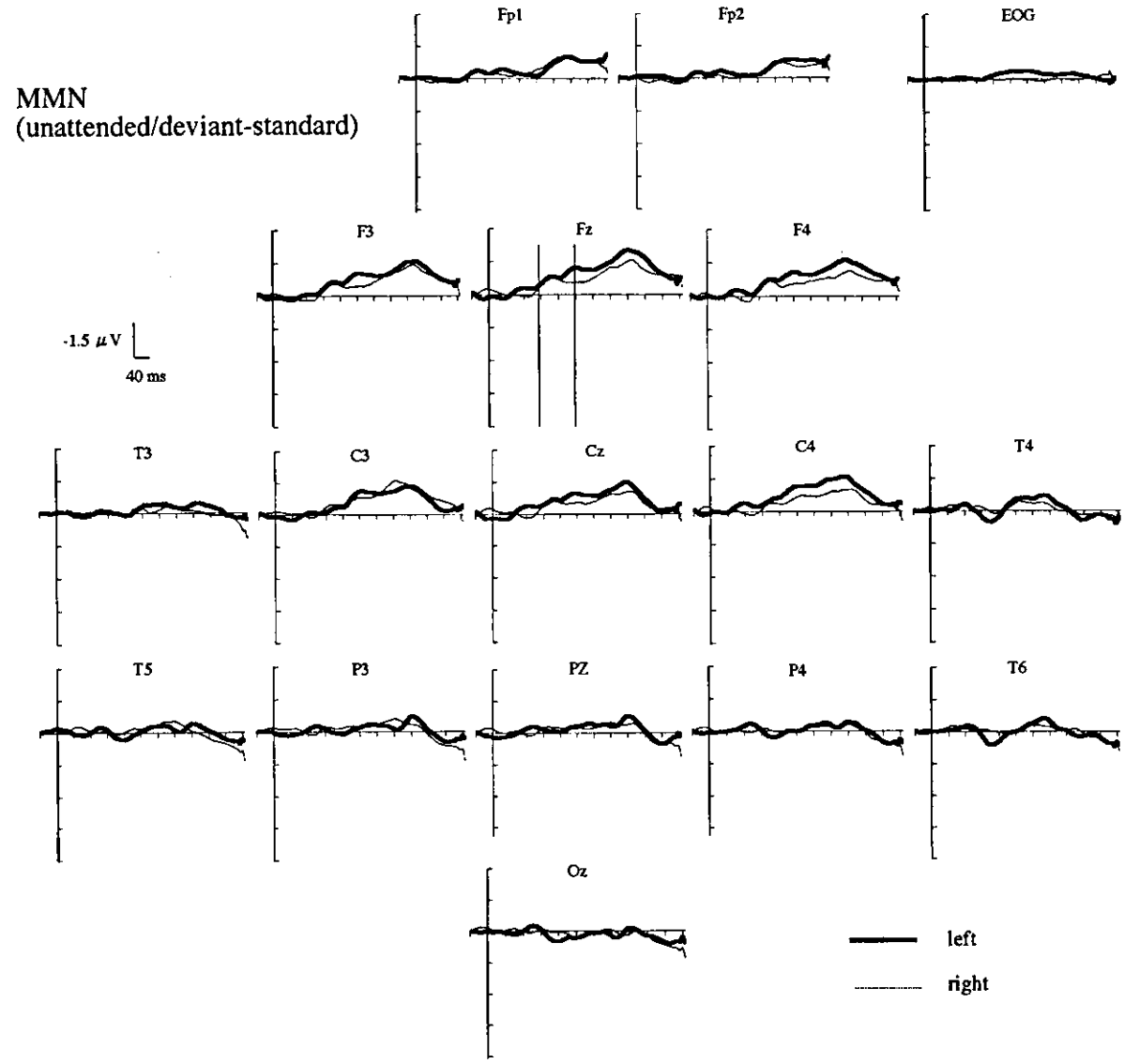

Fig. 1. Subtracted (unattended/deviant minus standard) grand-averaged ERP waveforms for the left ear of stimulation (*thick line*) and right ear of stimulation (*thin line*). Negativity is up. MMN amplitude was calculated as the mean amplitude within the time window of 120–200 ms indicated by the vertical lines at the Fz site. Note the polarity inversion observed between Fz and T6 in the same time window for MMN in response to the left ear stimuli.

those to the unattended tones, indicating that the subjects were allocating attention to the appropriate ear (Figs. 1–3). As shown in Fig. 1, sustained negative deflections were observed in the difference waveforms obtained by subtracting the ERPs to the standard tones from the deviant tones in the unattended condition at Fz for either ear of stimulation. However, the negativity inverted its polarity at T6 within the restricted latency range between 120 and 200 ms, notably for the left ear of stimulation, whereas the long-duration negativity later than 200 ms showed no polarity inversion between the electrode sites. Therefore, MMN was scored as the mean amplitude within the time

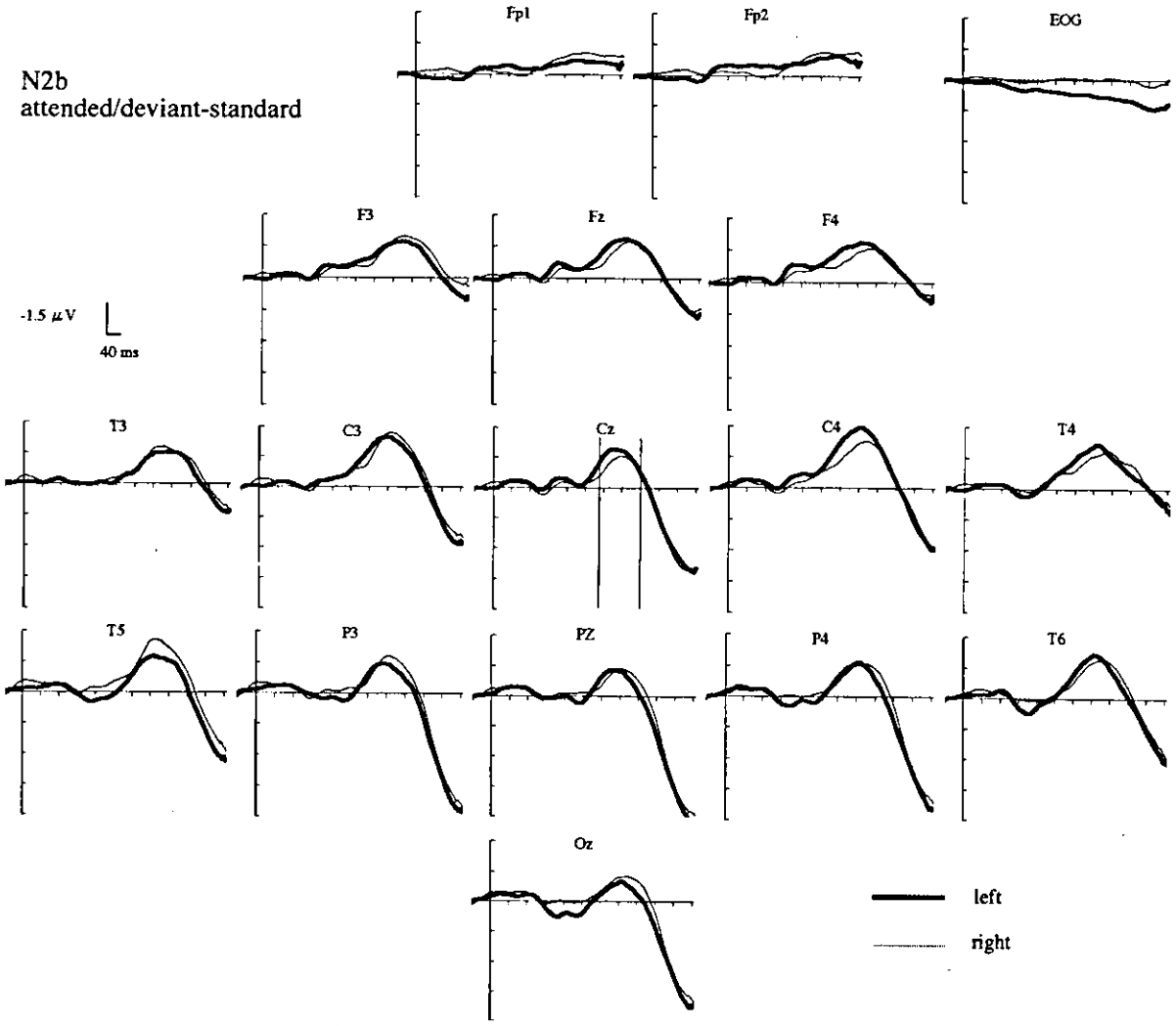

Fig. 2. Subtracted (attended/deviant minus standard) grand-averaged ERP waveforms for the left ear of stimulation (*thick line*) and right ear of stimulation (*thin line*). Negativity is up. N2b amplitude was calculated as the mean amplitude within the time window of 240–320 ms indicated by the vertical lines at the Cz site.

window of 120–200 ms. As shown in Fig. 4, topographic mapping of the MMN calculated by the mean amplitude within this time window shows a fronto-centrally distributed negativity and temporo-occipital positivity, which is consistent with previous findings. Visual inspection of the topographical mappings indicated that the negative focus in the frontal region was slightly deviated to the contralateral hemiscalp of the ear of stimulation. A repeated-measures ANOVA on the vector-normalized data of mean amplitudes at the two lateral frontal electrodes (F3, F4) was performed using the electrode and the stimulated ear as intra-individual factors. However, the interaction between the electrode and ear of stimulation did not reach a statistically significant level, suggesting that contralateral predominance of the MMN was not statistically demonstrated.

N2b was obtained by subtracting the ERPs to the standard tones from those to the deviant tones

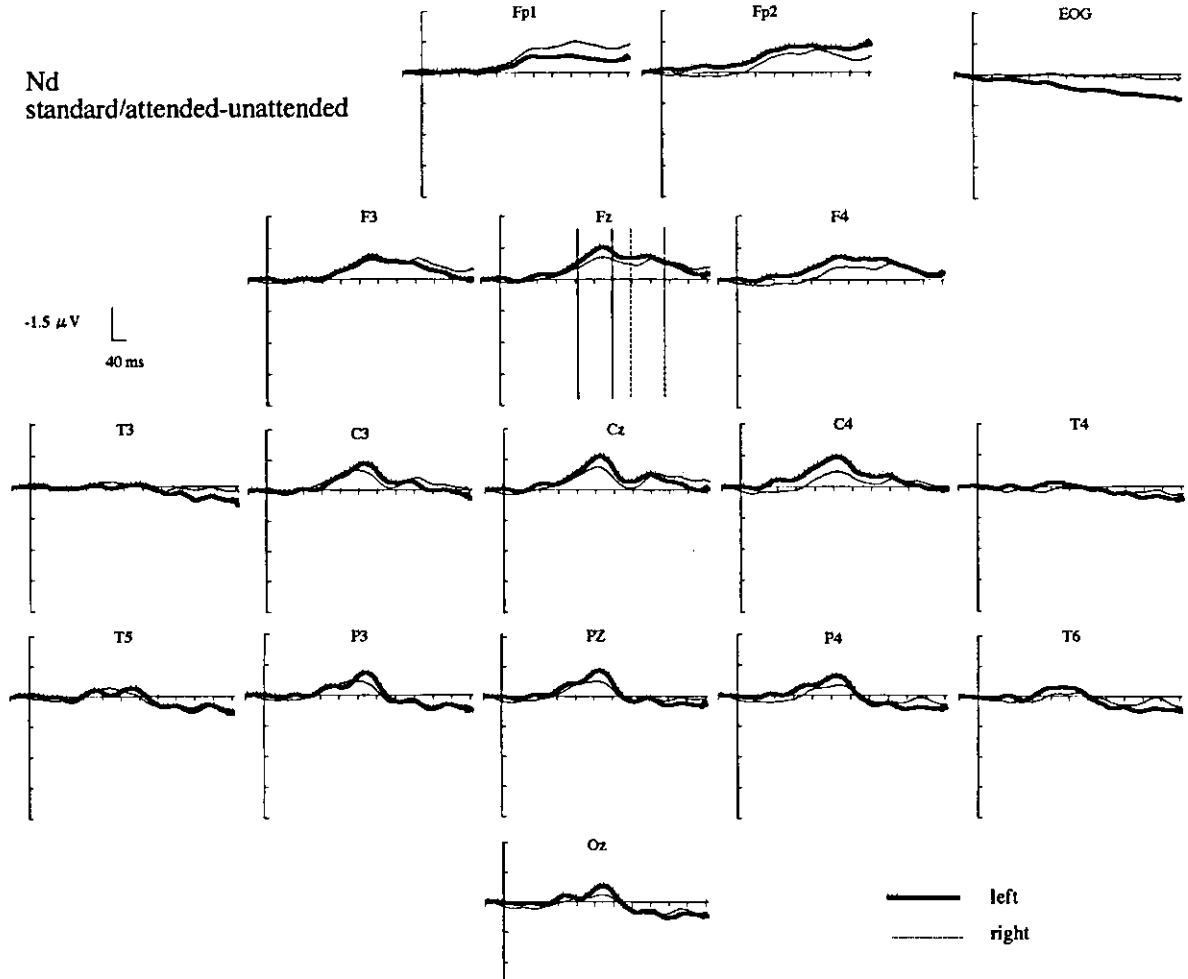

Fig. 3. Subtracted (standard/attended minus unattended) grand-averaged ERP waveforms for the left ear of stimulation (*thick line*) and right ear of stimulation (*thin line*). Negativity is up. Nde amplitude was calculated as the mean amplitude within the time window of 200–280 ms and Ndl amplitude within the time window of 320–400 ms indicated by the vertical lines at the Fz site.

in the difference waveform in the attended condition. The scalp distribution of the N2b, calculated as the mean amplitudes within the time window of 240–320 ms in the difference waveform by subtracting the ERPs to the standard stimuli from those to the deviant stimuli in the attended condition, also suggested a contralateral predominance to the stimulated ear in the central region. Again, repeated-measures ANOVA on the vector-normalized data of mean amplitudes at the four lateral electrodes (T3, C3, C4, T4) was performed using the hemiscalp (left, right) and electrode site (temporal, central) within each hemiscalp, and ear of stimulation as intra-individual factors. There was a significant interaction between hemiscalp and ear of stimulation [$F(1,18)=9.54$, $P=0.0063$]. A separate analysis for each ear of stimulation revealed that a significant main effect of hemiscalp was obtained for the left ear stimuli [$F(1,18)=4.73$, $P=0.0432$], but not for the right ear stimuli, which partly supports the view of contralateral predominance of N2b.

Two negative peaks were observed in the difference waveforms obtained by subtracting the ERPs to the standard stimuli in the unattended condition from those in the attended condition. The early negativity (Nde) ranging in the time window of 160–240 ms showed a fronto-centrally dominant

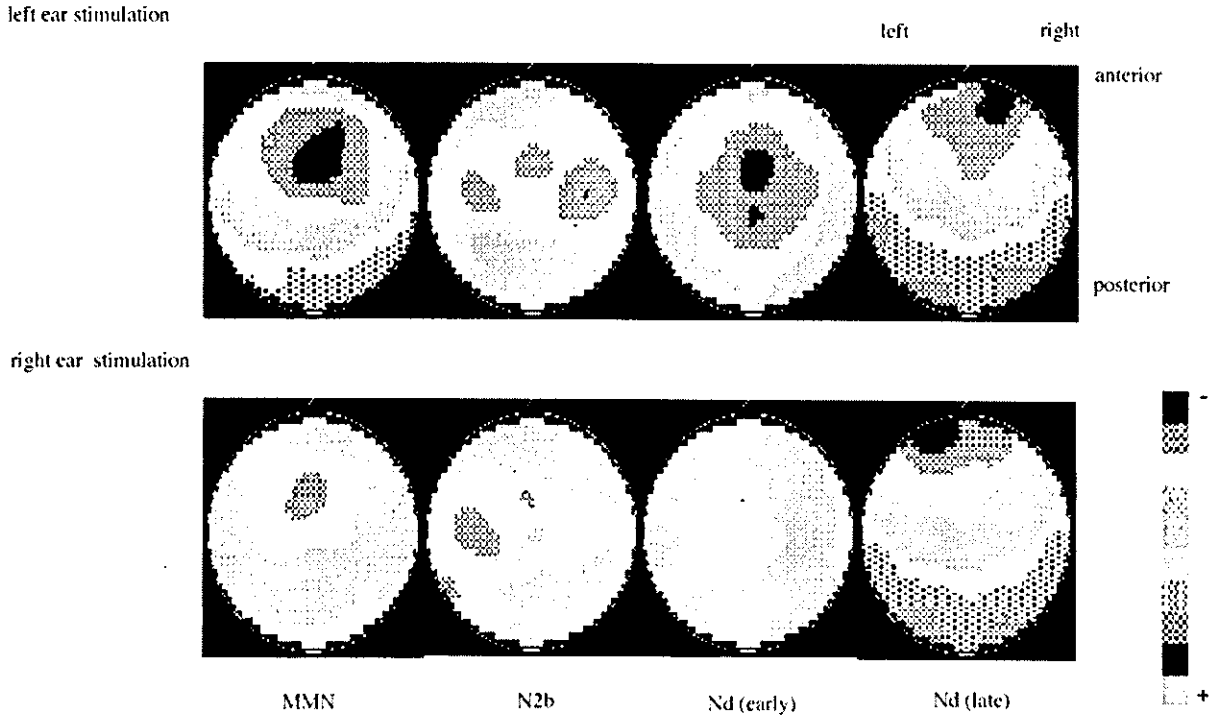

Fig. 4. Topographical mappings of each component labeled below. Potential mappings were calculated according to the method of spherical spline interpolation (Perrin et al., 1989), using the mean amplitude within the time window determined for each component at 16 electrode sites. As is shown in the scale bar, blue indicates negativity and red indicates positivity. Note the contralateral predominant distribution of N2b to each stimulated ear.

distribution, whereas the scalp distribution of the late negativity (Ndl) ranging in the time window of 280–360 ms was skewed to the anterior prefrontal sites, consistent with previous findings (Hansen and Hillyard, 1980, 1984; Okita et al., 1983). Repeated-measures ANOVA on the vector-normalized data of mean amplitudes at the four midline electrodes (Fz, Cz, Pz, Oz) for each time window was performed using the electrode, time window and ear of stimulation as intra-individual factors. A significant interaction between electrode and time window suggested that Ndl was significantly more anteriorly distributed compared with Nde [$F(3,54)=25.13$, $\varepsilon=0.63$, $P=0.0001$].

3.3. Relation between ERP indices and CPT sensitivity A′

Spearman rank correlation coefficients were calculated between CPT sensitivity A′ and ERP scores measured in the electrode sites where each component was clearly elicited (Table 2). The electrode sites adopted for analysis were: F3, Fz and F4 for MMN; F3, Fz, F4, T3, C3, Cz, C4 and T4 for N2b; Fz, C3, Cz and C4 for Nde; and Fp1, Fp2 and Fz for Ndl. Taking into account the multiple analyses to be performed, the significance level (α level) was corrected to $P=0.01$. Among the ERP scores measured in the electrode sites noted above, only N2b at Fz, F4, Cz, C4 and T4 to the right stimulated ear showed significant positive correlations with CPT sensitivity A′.

Moreover, the counting performance in the ERP task for either stimulated ear showed a positive correlation with the CPT sensitivity A′ (left stimulated ear, $r=0.52$, $P=0.02$; right stimulated ear, $r=0.74$, $P=0.003$). Additional correlational analyses between the counting performance in the ERP task and the ERP scores were performed separately for each stimulated ear, which revealed positive

Table 2
Spearman rank correlation coefficients between CPT sensitivity A', counting performance in the ERP task and ERP indices

			CPT sensitivity A'	ERP counting performance
Left	MMN	F3	0.38	−0.40
		Fz	0.25	−0.30
		F4	0.41	−0.36
	N2b	F3	0.34	−0.13
		Fz	0.26	0.11
		F4	0.16	0.02
		T3	0.13	−0.14
		C3	0.29	−0.11
		Cz	0.18	0.09
		C4	0.28	0.07
		T4	0.18	0.14
	Nde	Fz	0.13	0.11
		C3	0.07	0.06
		Cz	0.14	0.20
		C4	0.12	0.26
	Ndl	Fp1	0.18	−0.03
		Fp2	0.12	0.26
		Fz	0.27	−0.04
Right	MMN	F3	0.31	−0.19
		Fz	0.19	0.02
		F4	0.26	−0.14
	N2b	F3	0.48	−0.34
		Fz	0.64*	−0.57
		F4	0.59*	−0.43
		T3	0.25	−0.50
		C3	0.48	−0.67*
		Cz	0.60*	−0.55
		C4	0.75**	−0.63*
		T4	0.69**	−0.71**
	Nde	Fz	0.29	−0.30
		C3	0.32	−0.26
		Cz	0.18	−0.34
		C4	−0.17	0.07
	Ndl	Fp1	−0.05	0.23
		Fp2	−0.08	0.27
		Fz	−0.05	0.25

Note that the counting performance in the ERP task was calculated from the average rate of deviation of the counts from the number of targets for each ear of stimulation. Therefore, a negative correlation coefficient indicates that a higher absolute amplitude is associated with better performance level.

* $P<0.01$.

** $P<0.001$.

correlations between the performance level and N2b at C3, C4 and T4 to the right stimulated ear (C3, $r=0.67$, $P=0.002$; C4, $r=0.63$, $P=0.004$; T4, $r=0.71$, $P=0.0007$).

4. Discussion

The present study aimed to elucidate the psychophysiological factors related to CPT performance, using ERP indices reflecting different aspects of information processing. Although ERPs were not measured during the CPT task per se, the counting performance level in the auditory selective attention task for either stimulated ear showed a significant positive correlation with the CPT sensitivity A', indicating that the stimulus detection performance in both tasks probably shares a common feature of stimulus processing. Moreover, the counting performance for the right stimulated ear was more strongly correlated with the CPT sensitivity A' than that for the left stimulated ear. A number of interesting findings were obtained between the ERP indices and the CPT sensitivity A'.

Firstly, among the ERP indices investigated in the present study, only N2b showed a significant positive correlation with CPT sensitivity A', suggesting that controlled deviance detection capacity plays a relevant role in DSCPT performance, rather than automatic deviance detection or focused attention per se. In contrast to the CPT versions that use a fixed, clearly focused, single trial ('X' CPT) and/or sequential-trial target ('AX' CPT), CPT versions that use highly blurred stimuli (DSCPT) have been found to show no significant practice effects, which raises the possibility that the DSCPT might be resistant to the development of automaticity and owe much to controlled processing (Nuechterlein et al., 1991). Controversy remains about the functional significance of N2b. Some studies suggest that N2b reflects allocation of effort to detect deviance, arising from the finding that N2b increases with discrimination difficulty (Fitzgerald and Picton, 1983; Näätänen and Picton, 1986), but not all studies show this (Sams et al., 1985; Novak et al., 1990; Schröger, 1995). Moreover, there is another view that N2b reflects the attention switching process and is supported by